Understanding the Effects of Heat Treatment

Temperature and Atmosphere on Platinum

Nanoparticles Sintering Processes on Different

Engineered Catalyst Supports (ECS<sup>TM</sup>) for Fuel Cell

Applications

Andres O. Godoy<sup>1</sup>, Jayson. Foster<sup>2</sup>, Mikaela Dicome<sup>3</sup>, Geoff McCool<sup>3</sup>, Barr Zulevi<sup>3</sup>, Michele Ostraat<sup>3</sup>, Svitlana Pylypenko<sup>2</sup>, and Jasna Jankovic<sup>1,\*</sup>.

<sup>1</sup>Institute of Materials Science, University of Connecticut, Storrs, Connecticut 06269, United States. <sup>2</sup>Department of Chemistry, Colorado School of Mines, Golden, Colorado 80401, United States. <sup>3</sup>Pajarito Powder, LLC, Albuquerque, New Mexico 87109, United States.

\*Corresponding Author

KEYWORDS: Catalyst, heat treatment, PEM, porosity, surface area, sintering, particle growth.

**ABSTRACT:** Proton exchange membrane (PEM) fuel cells are highly efficient devices for the conversion of chemical energy into electricity and are a promising candidate to sustain the growing clean energy demands. However, tunability of the catalyst materials used in their electrodes is necessary to meet specific applications and to address some of the major challenges of this technology. In this work, we present a study on the effects of post-synthesis heat treatments on tunable PEM catalyst materials, containing 30 wt.% Pt deposited on two different types of engineered catalyst supports (ECS<sup>TM</sup>) having different degrees of porosity and surface area. The role of temperature and atmosphere on the properties of these catalyst materials was studied by performing heat treatments at temperatures ranging from 400°C to 1000°C and in three different atmospheres of 7% H<sub>2</sub>/N<sub>2</sub>, N<sub>2</sub>, and Ar, followed by evaluation of the changes in Pt nanoparticle and carbon support properties by a wide range of physicochemical characterization techniques. The study showed that the temperature was the main driving force for the structural changes in the catalyst material, while the different atmospheres affected the Pt surface oxidation state. This work highlights the importance of studying catalyst properties during the stages of catalyst fabrication, a topic that has not been extensively reported.

#### 1. INTRODUCTION

High emissions of pollutants that are produced from fossil fuel-based energy generation have triggered not only a climate and an environmental crisis but also a growing demand for clean and efficient energy sources<sup>1,2</sup>. Polymer electrolyte membrane fuel cells (PEMFCs) are one of the most advantageous solutions for clean energy applications due to their near-zero-emission, high efficiency, low maintenance cost, and high energy density<sup>2,3</sup>. The basic principle behind PEMFCs is to produce electricity through the electrochemical reactions of hydrogen and oxygen (or air) taking place in a membrane electrode assembly (MEA) by converting the chemical energy of the hydrogen oxidation reaction (HOR) and oxygen reduction reaction (ORR) into electrical energy, with water as a byproduct<sup>4,5</sup>. The catalyst materials used in this technology have the essential role of accelerating the rate of HOR at the anode and ORR at the cathode. Pt or Pt-based alloy nanoparticles (NPs) distributed on a carbon support, in both the anode and the cathode, are the PEMFCs state-of-the-art catalyst material<sup>6,7</sup>. This is due to Pt's low overpotential for HOR and ORR and its stability in harsh PEMFC operating conditions, as well as the carbon's large surface area and good electronic conductivity. The Pt and carbon support interaction play a significant role in the electrocatalytic properties of the catalyst material<sup>8,9</sup>. However, the ORR at the cathode is a slower reaction, compared to the HOR at the anode, and for this reason higher Pt loading at the cathode is needed to compensate for the sluggish ORR kinetics<sup>10</sup>. Fabrication of ORR catalysts with high performance at scale is still a challenge that needs to be tackled to enable a marketable increase of the energy generated from this technology. The tunability of the catalyst materials in terms of catalyst support morphology, porosity, Pt catalyst distribution and loading is essential to meet energy demands for specific applications<sup>11,12</sup>.

Generally, the structure of the carbon supports is tailored to provide properties necessary to improve the performance in a plethora of applications, such as fuel cells, hydrogen storage, absorbent materials, batteries, supercapacitors, etc. 13. Due to their important role in fuel cells, a number of studies have been focused on tuning the carbon properties for enhanced catalyst/support interaction and fuel cell performance<sup>14–28</sup>. For example, Asset et al. 15 demonstrated the influence of the texture, structure, and chemistry of different carbon supports (carbon blacks, carbon nanotubes, graphene nanosheets) in controlling the morphology, size, and Ni content of porous hollow PtNi/C. They observed a decrease in the diameter of the catalyst NPs by increasing the carbon mesopore surface area. In previous studies, Ismagilov et al<sup>16</sup>, synthesized a variety of amorphous "super-microporous" carbons (ASC), made from different organic precursors, for PEMFC platinum cathode catalysts. From their findings the catalysts supported on ASC performed better in MEA than catalyst supported on conventional carbon black. More recently, Gu et al. 17 studied the effect of tunable porosity in mesoporous carbon used as the catalyst support for enhanced PEMFC performance and improved durability. They showed that an optimal porosity allows for better dispersion of the catalytic material and prevents catalyst agglomeration. Similarly, by using a tunable porous carbon support, Marie et al. 18 concluded that the structure of the carbon support has a major role in the structure of the catalytic layer and the mass-transport processes in PEMFC cathodes. Counterintuitively, they found that as the pore size of the carbon support increases, the porosity of the resulting catalytic layer is reduced. This is due to the Nafion penetration into the large pores of the carbon support provoking high proton resistance and masstransport losses in tested MEA. Later on, Ouattara et al. 19 further confirmed this effect by controlling the carbon support architecture to reduce mass-transport voltage losses. They observed that the carbon texture can significantly limit the gas diffusion process and the MEA performance.

Kaluža et al.<sup>20</sup> reported on different carbon black supports with medium surface area (~400 m<sup>2</sup>/g) showing better electrochemical stability than the commercial high-surface-area reference catalyst. Besides the implementation of a mesoporous carbon network, changing the carbon graphitization degree and functionalization or doping of the carbon sp<sup>2</sup> hybridized network (with elements like nitrogen, sulfur, boron or other heteroatoms) are other avenues to tune the carbon support properties and enhance its electrochemical behavior<sup>21–24</sup>. The addition of dopant atoms modifies the electronic structure of the carbon matrix, the nucleation and kinetic growth of the catalyst NPs, as well as the nature of the catalyst-support interactions, creating a more homogeneous catalyst distribution and in some cases smaller catalyst particle sizes<sup>25</sup>. A notable work by Kim et al.<sup>26</sup> reported preparation of Pt NPs on functionalized and graphitized carbon support using in situ grafting of the trifluoro-methylphenyl groups to enhance the durability and activity of the catalytic material by means of a direct attachment of functional groups. The researchers found that the obtained p-conjugated carbon structure resulted in a reduced contact resistance between Pt and carbon and an improved dispersion of Pt NPs on the graphitized carbon surfaces. Urchaga et al.<sup>29</sup> revealed that, compared to commercial catalysts, Pt crystallite growth can be delayed by altering the carbon surface with thiophenol groups during heat treatments at 200°C under a hydrogen atmosphere. This resulted in improved Pt-to-substrate interaction, better Pt stability under a hydrogen atmosphere, and lower loss of ECSA during electrochemical aging. In general, carbon support for fuel cells can be modified by specific fabrication and post-treatment methods when certain characteristics are required, such as precise carbon composition, enhanced graphitization degree, desirable surface functionalities, optimal concentration and identity of surface defects, specific pore size or design, high surface area, tailored morphology, among others<sup>27,28</sup>.

Pt NPs distribution on engineered and other carbon supports very much affects the catalyst activity. As mentioned above, enhanced and high dispersion of small particles is desired for high electrochemically active surface area (ECSA). However, Pt NP catalysts often experience conditions that causes growth and agglomeration, either during catalyst synthesis or PEMFC operation<sup>30,31</sup>. This is a result of the size-dependent properties of nano-sized Pt catalyst, which are different from the bulk macrostructures, and its inherent tendency to agglomerate and grow into larger particle sizes driven (mainly) by reduction of high surface energy<sup>32</sup>. The decrease of the surface energy, induced by the NP growth, can slow the growth rate with time. Additionally, the degradation mechanisms that these catalyst materials experience during PEMFC operation or after lab-based accelerated stress tests have already been extensively studied. It is well known that combined Ostwald ripening, Pt growth/agglomeration, Pt migration, Pt dissolution, and Pt2+ ion transport, are the most predominant degradation mechanisms for Pt NPs in PEMFCs, inducing its growth, reducing its ECSA and therefore lowering the PEMFC performance<sup>33,34</sup>. However, it is also important to study the phenomena and the factors that accelerate Pt growth and agglomeration during the catalyst fabrication stages, especially when heat treatments are involved. The catalyst synthesis approach, the carbon support characteristics and the heat treatment temperatures and atmospheres can determine the resulting properties of the catalyst material and its catalytic efficiency in PEMFC<sup>35,36</sup>. Understanding the effect that these conditions have on the catalyst material can help to better engineer catalyst NPs size and distribution, as well as carbon support materials at large scale, and fabricate efficient, corrosion-resistant and durable catalysts. This can be achieved by altering and enhancing the catalyst/support interaction and the physical characteristics of the carbon support, such as the porosity and the degree of graphitization, as well as the catalyst material, such as the size, distribution and morphology of the NPs, resulting in better dispersed Pt NPs. An improved catalyst design would enable higher ECSA, electron transfer, diffusion of chemical species and a decrease of the catalyst loading<sup>37,38</sup>. Therefore, controlling the size, dispersion, and morphology of Pt NPs during catalyst synthesis is a key factor to developing enhanced PEMFC with improved performance.

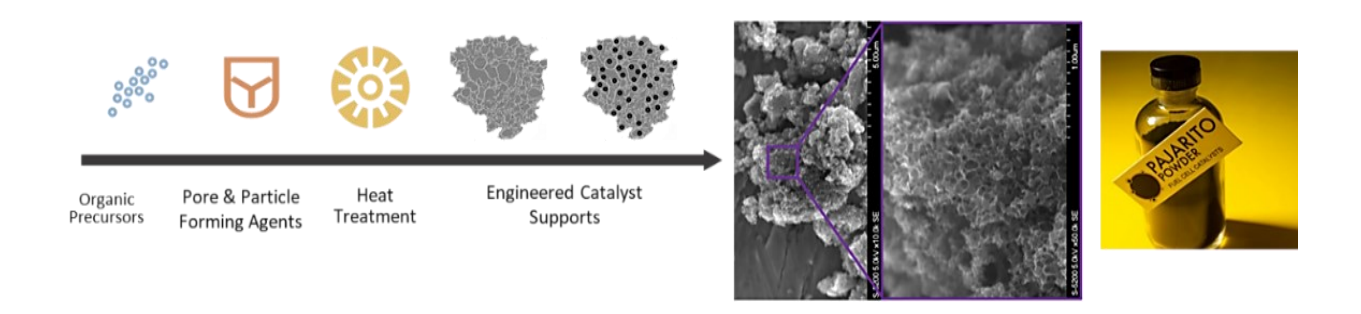


**Figure 1.** Schematic of Pajarito Powder's VariPore<sup>™</sup> process diagram, SEM image of catalyst morphology and photography of catalyst powder [images reproduced with permission from Pajarito Powder, LLC<sup>39</sup>. Copyright (2023)]

In this research, we are focusing on commercial tunable carbon supports, namely Engineered Catalyst Supports (ECS<sup>TM</sup>), produced by Pajarito Powder, LLC, a manufacturer of advanced catalysts materials for PEM and alkaline fuel cells and electrolyzers, see Figure 1. These ECS<sup>TM</sup> materials, made of inexpensive and available materials, are manufactured by the proprietary VariPore<sup>TM</sup> process. This work investigated the sintering and agglomeration processes that take place during post synthesis treatments. Specifically, we report our findings on the effect of heat treatments and different atmospheres on controlling the physical characteristics of these catalysts, like the carbon support morphology, catalyst surface chemistry, and the catalyst particle size distribution. This understanding can help develop catalysts with enhanced activity and durability,

improving the fuel cell performance, extending the working life, and reducing the cost of fuel cells for the most demanding applications, including heavy-duty fuel cell vehicle applications.

#### 2. EXPERIMENTAL

## 2.1. Heat treatment:

Two different as-prepared catalysts, containing 30 wt.% Pt supported on two types of Engineered Catalyst Supports ECS<sup>TM</sup> (Pajarito Powder LLC), namely ECS<sup>TM</sup> 3701 and ECS<sup>TM</sup> 4601, were used in this study. Both powders were heat treated in three different atmospheres; and at a range of temperatures. A tube furnace, Lindberg/Blue from Thermo Fisher Scientific with a super OMEGACLAD<sup>TM</sup> Thermocouple and a quartz tube of 7.4 cm D x 121.9 L cm (~5250 cm³) was used to heat treat ~ 0.5 gr of the catalyst material. The heat treatment was performed at different temperatures ranging from 400°C to 1000°C at a 10°C/min ramp rate and in three different atmospheres, a 7% H<sub>2</sub>/N<sub>2</sub> mixture, N<sub>2</sub>, and Ar for 1 hr at 0.5 scfh flow rate. Ultra-high purity (99.999%) N<sub>2</sub> and Ar gases were used. N<sub>2</sub> gas flow was used, for 30 min, to purge air from the tube furnace and the powders before starting the heat treatments, and later to purge the treatment gases from the tube once the heat treatments were finished.

## 2.2. Physicochemical Characterization:

<u>X-ray diffraction (XRD):</u> The characterization of the crystal structures and graphitic nature of the samples was performed using XRD on a Rigaku MiniFlex 600 with mono-chromated Cu K $\alpha$  radiation ( $\lambda = 1.5406$  Å) in a shallow sample dish. The crystallite sizes were estimated based on the prominent facets of the crystallites and the width of their peak reflections in the spectrums. The mean Pt crystallite sizes were calculated using Scherrer's equation (see Equation 1), where  $\beta$  is

the full width at half maximum (FWHM) of the diffraction peak in radians, and  $\lambda = 0.15406 \ nm^{40}$ .

Scherrer's equation 
$$L = \frac{0.9\lambda}{\beta \cos \theta}$$
 Equation 1

CO Chemisorption: The calculation of the Pt metallic surface area was performed using carbon monoxide (CO) as the adsorbate gas in pulse chemisorption. The experiment was conducted by sending pulses of CO to a reactor until complete saturation of the catalyst sites was reached. The amounts of CO chemisorbed selectively on Pt catalytic sites were measured on a Micromeritics Autochem 2920 instrument and the analysis was performed at a temperature-programmed reduction (TPR) of 473.15 K (200°C) and a pulse chemisorption temperature of 308 K (35°C) with a flow rate of 50 cm<sup>3</sup> STP/min.

Raman Spectroscopy: The evaluation of carbon structure was conducted using a Thermo DXR2 Raman spectrometer equipped with a 532 nm diode laser with a power of 6 mW and a 50 µm pinhole aperture for sample illumination and collection of the scattered photons. Five different scans were collected from a 20 ml glass vial filled with catalyst powder. Standard background subtraction was used to remove the glass vial contribution to the spectrum. The fitting of the obtained Raman spectra considers the presence of two main first-order peaks, D1 and G. The variation of their widths and relative intensities were used to characterize the degree of carbon graphitization<sup>41</sup>. To study and quantify the changes in the graphitization degree of the carbon support structure after heat-treatments, the relative intensity ratios, R, of the integrated intensities of the disorder-induced D1 and G Raman bands (I<sub>D1</sub> and I<sub>G</sub>) was used, see Equation 2<sup>42</sup>. The Knight and White equation was used to calculate carbon's crystallite sizes, La<sup>43</sup>, see Equation 3.

Relative intensity ratios 
$$R = \frac{I_{D1}}{I_G}$$
 Equation 2

Knight and White equation 
$$\frac{I_{D1}}{I_G} = \frac{4.4}{L_a}$$
 Equation 3

N<sub>2</sub> Physisorption: Catalyst porosity, pore size distribution and specific surface area were analyzed using physical adsorption of nitrogen at the liquid-nitrogen temperature of 77 K (-196°C) on a Micromeritics ASAP 2020 Accelerated Surface Area and Porosimetry Analyzer. Before measurements and analysis, the samples were degassed at 573K (300°C) for 6 hr at vacuum. The specific surface areas were acquired using the Brunauer-Emmett-Teller (BET) method, based on a model of monolayer-multilayer adsorption, with a relative pressure range of  $\sim 0.1-0.15$ . Since the BET model fails to accurately describe adsorption in micropores<sup>44</sup>, the volume and sizes of the pores were calculated using the Barrett-Joyner-Halenda (BJH) method for the adsorption branches. The maximum positions of the BJH curves were used to estimate pore-size distributions and the volume of nitrogen adsorbed at a P/Po  $\sim 0.99$  was used to calculate the total pore volumes. A note that BJH and BET methods were used for the carbon surface evaluation because these are the most traditional methods currently used to perform such evaluation<sup>45–47</sup>. According to Borghi et al. 48 gas adsorption is the customary technique of choice to characterize the porosity and specific surface area of porous carbons. It allows the scrutiny of a wide range of pore sizes from micro to macro pores (< 2 nm up to a few hundred nanometers), while the pore size distribution and the total pore volume can be characterized using the BJH. However, it may not be possible to accurately describe the sizes of micropores using methods based on the Kelvin equation such as

BJH. The quenched solid density functional theory (QSDFT) and non-local density functional theory (NLDFT) method would be a more appropriate approach. These approaches assume the corrugation of the carbon surface. Despite this, the BJH method is a good choice when the identification of the porosity range is the main target for evaluation, as in our study.

Transmission Electron Microscopy (TEM): TEM was used to further investigate morphological and structural characteristics of the catalyst materials and to analyze Pt NP dispersion and size distribution. TEM was conducted in a Thermo Scientific<sup>TM</sup> TalosF200×200 kV D6329 XTwin TEM, using bright field TEM (BF-TEM) mode. Before imaging, the samples were first dispersed in 50 v/v % of isopropyl alcohol and distilled water, then ultrasonicated using a 2510R-DTH BransonicR Ultrasonic Cleaner for 15–30 min (130 W, 40 kHz) and deposited on a 300 mesh lacey carbon-coated Cu grid for TEM characterization, followed by drying for 30 min under an infrared lamp. The TEM micrographs were used to calculate the average particle size distribution (PSD) of the electrocatalysts metal from the number-averaged mean-particle size was calculated using Equation 4, where  $d_N$  is the averaged mean particle size and  $n_i$  is the number of particles of size  $d_i$ . Additionally, Fast Fourier transform (FFT) was used to analyze the high resolution BF-TEM using the Gatan microscopy suite, Digital Micrograph.

Averaged mean particle size 
$$\overline{d_N} = \sum_{i=1}^n n_i d_i / \sum_{i=1}^n n_i$$
 Equation 4

X-ray Photoelectron Spectroscopy (XPS): XPS was used to study the surface elemental and chemical composition of as-received and post-treated materials. The measurements were

performed using a Scienta-Omicron HiPP-3 system equipped with an R4000 hemispherical energy analyzer, calibrated to the Au  $4f_{7/2}$  region at 83.95 eV of a sputter-cleaned Au foil. Measurements were collected with high-voltage lenses in the swift acceleration operating mode. An Al K $\alpha$  X-ray source was operated at 300 W with a  $\sim$  900  $\mu$ m spot size, and all core level spectra were taken at a combination of a 200 eV pass energy and a 0.8 mm  $\times$  30 mm slit size resulting in an estimated energy resolution of 0.6 eV. The analysis chamber pressure was maintained at a level below  $5.0\times10^{-8}$  mbar, while the analyzer pressure remained below  $1\times10^{-9}$  mbar. Samples were mounted on conducting carbon tape and therefore no charge referencing was necessary. Spectral processing was performed using CasaXPS software, where a Shirley background was applied to the Pt 4f and C 1s core levels.

## 3. RESULTS AND DISCUSSION:

Summary of all psychochemical characterization results for bare ECS<sup>TM</sup> materials, baseline catalyst (as fabricated platinized catalyst, prior to heat-treatment) and heat-treated catalysts is given in Table 1 and Figure 2.

**Table 1.** Physical and structural characterization.

Material	XRD Pt Crystallite size, L (nm)	XRD ECS <sup>TM</sup> d <sub>002</sub> - spacing (Å)	CO Metallic Surface Area (m²/g)	Raman ID/IG	BET Surface Area (m²/g)	BJH Pore Volume (cm³/g)	BJH Pore Diameter (nm)	TEM Pt $d_{\scriptscriptstyle N}$ (nm)	FFT/TEM Pt Interplanar spacing <sup>®</sup> d(111) (Å)
Bare ECS <sup>TM</sup> 3701	n/a	3.45	n/a	1.02	732	1.72	12.4	n/a	n/a
30%Pt/ECS <sup>TM</sup> 3701, Baseline	1.51	3.47	119	0.99	587	1.19	11.8	2.49	2.26

1.57	3.51	111	1.05	597	1.30	12.1	2.56	n/m
5.36	n/m	43.7	1.08	618	1.36	12.0	5.37	2.25
2.06	3.50	106	0.99	578	1.11	11.4	2.54	n/m
4.70	n/m	47.8	1.08	613	1.19	11.9	5.09	2.26
2.07	3.52	108	1.01	588	1.17	11.8	2.46	n/m
4.63	n/m	50.5	1.13	607	1.24	11.9	5.36	2.26
n/a	3.48	n/a	1.04	873	2.19	13.3	n/a	n/a
1.69	3.51	110.9	1.01	667	1.55	12.8	2.46	2.27
2.14	3.52	100.8	1.02	658	1.37	11.7	2.68	n/m
5.11	n/m	36.0	1.08	710	1.69	12.7	5.42	2.27
2.11	3.53	35.1	1.01	644	1.40	12.4	4.55	n/m
4.47	n/m	14.7	1.08	666	1.59	12.8	4.87	2.28
2.11	3.52	94.8	1.01	618	1.43	12.9	2.89	n/m
4.45	n/m	64.2	1.07	650	1.54	12.4	5.62	2.28
	5.36 2.06 4.70 2.07 4.63 n/a 1.69 2.14 5.11 2.11 4.47	5.36 n/m  2.06 3.50  4.70 n/m  2.07 3.52  4.63 n/m  n/a 3.48  1.69 3.51  2.14 3.52  5.11 n/m  2.11 3.53  4.47 n/m  2.11 3.52	5.36       n/m       43.7         2.06       3.50       106         4.70       n/m       47.8         2.07       3.52       108         4.63       n/m       50.5         n/a       3.48       n/a         1.69       3.51       110.9         2.14       3.52       100.8         5.11       n/m       36.0         2.11       3.53       35.1         4.47       n/m       14.7         2.11       3.52       94.8	5.36       n/m       43.7       1.08         2.06       3.50       106       0.99         4.70       n/m       47.8       1.08         2.07       3.52       108       1.01         4.63       n/m       50.5       1.13         n/a       3.48       n/a       1.04         1.69       3.51       110.9       1.01         2.14       3.52       100.8       1.02         5.11       n/m       36.0       1.08         2.11       3.53       35.1       1.01         4.47       n/m       14.7       1.08         2.11       3.52       94.8       1.01	5.36       n/m       43.7       1.08       618         2.06       3.50       106       0.99       578         4.70       n/m       47.8       1.08       613         2.07       3.52       108       1.01       588         4.63       n/m       50.5       1.13       607         n/a       3.48       n/a       1.04       873         1.69       3.51       110.9       1.01       667         2.14       3.52       100.8       1.02       658         5.11       n/m       36.0       1.08       710         2.11       3.53       35.1       1.01       644         4.47       n/m       14.7       1.08       666         2.11       3.52       94.8       1.01       618	5.36       n/m       43.7       1.08       618       1.36         2.06       3.50       106       0.99       578       1.11         4.70       n/m       47.8       1.08       613       1.19         2.07       3.52       108       1.01       588       1.17         4.63       n/m       50.5       1.13       607       1.24         n/a       3.48       n/a       1.04       873       2.19         1.69       3.51       110.9       1.01       667       1.55         2.14       3.52       100.8       1.02       658       1.37         5.11       n/m       36.0       1.08       710       1.69         2.11       3.53       35.1       1.01       644       1.40         4.47       n/m       14.7       1.08       666       1.59         2.11       3.52       94.8       1.01       618       1.43	5.36       n/m       43.7       1.08       618       1.36       12.0         2.06       3.50       106       0.99       578       1.11       11.4         4.70       n/m       47.8       1.08       613       1.19       11.9         2.07       3.52       108       1.01       588       1.17       11.8         4.63       n/m       50.5       1.13       607       1.24       11.9         n/a       3.48       n/a       1.04       873       2.19       13.3         1.69       3.51       110.9       1.01       667       1.55       12.8         2.14       3.52       100.8       1.02       658       1.37       11.7         5.11       n/m       36.0       1.08       710       1.69       12.7         2.11       3.53       35.1       1.01       644       1.40       12.4         4.47       n/m       14.7       1.08       666       1.59       12.8         2.11       3.52       94.8       1.01       618       1.43       12.9	5.36       n/m       43.7       1.08       618       1.36       12.0       5.37         2.06       3.50       106       0.99       578       1.11       11.4       2.54         4.70       n/m       47.8       1.08       613       1.19       11.9       5.09         2.07       3.52       108       1.01       588       1.17       11.8       2.46         4.63       n/m       50.5       1.13       607       1.24       11.9       5.36         n/a       3.48       n/a       1.04       873       2.19       13.3       n/a         1.69       3.51       110.9       1.01       667       1.55       12.8       2.46         2.14       3.52       100.8       1.02       658       1.37       11.7       2.68         5.11       n/m       36.0       1.08       710       1.69       12.7       5.42         2.11       3.53       35.1       1.01       644       1.40       12.4       4.55         4.47       n/m       14.7       1.08       666       1.59       12.8       4.87         2.11       3.52       94.8       1.01<

Physical and structural characterization of bare ECS<sup>TM</sup> and 30%Pt /ECS<sup>TM</sup> catalysts, before and after treatment. All values given in the table are average taken from 5 to 10 different measurements. Symbols and abbreviations: Not applicable (n/a); Not measure (n/m); @Pt d(111) represents the interplanar distance at the most prominent reflection on these Pt NPs.

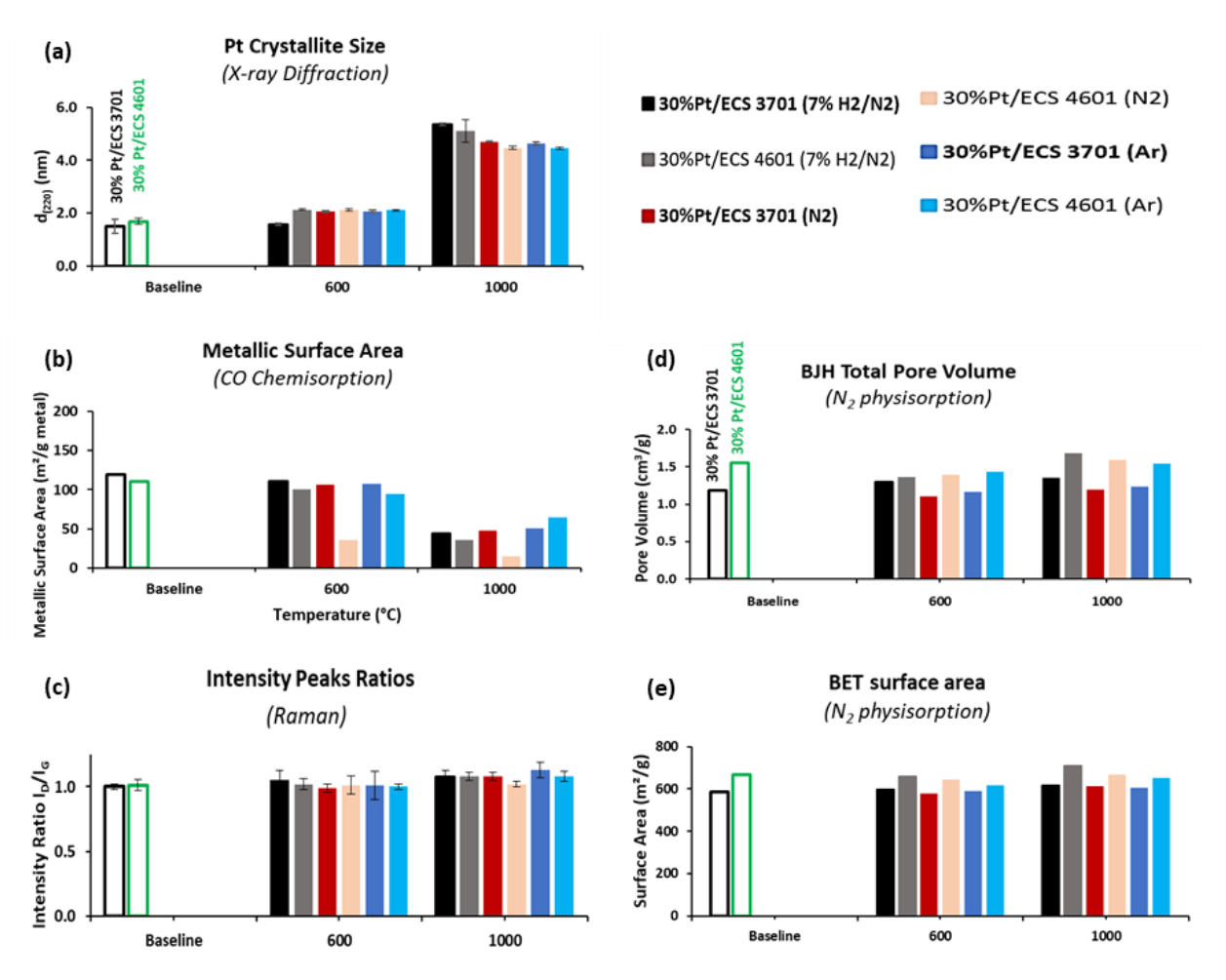


**Figure 2.** Column charts of physical and structural characterization plots of catalysts 30%Pt deposited on ECS<sup>TM</sup>, before and after treatment: (a) Crystallite sizes based on XRD at (220) Pt interplanar spacing, (b) metallic surface area taken from CO chemisorption, (c) Raman intensity ratios, (d) BJH porosity taken from N<sub>2</sub> physisorption, (e) BET surface area taken from N<sub>2</sub> physisorption.

Before heat treatments in different atmospheres, a large set of ECS<sup>TM</sup> catalyst powders with different Pt loadings were heat-treated at different temperatures from room temperature to above 1000°C in a 7% H<sub>2</sub>/N<sub>2</sub> atmosphere. The Pt crystallite growth was measured from X-ray diffraction (XRD) data with equation 1. No particular Pt growth was observed until 400°C. However, an

accelerated growth rate was observed for all catalysts at temperatures  $\geq 500^{\circ}$ C, see Figure 3. This is in agreement with Bett et al.<sup>49</sup> who confirmed that for substantial Pt crystallite growth on carbon support, temperatures exceeding 600°C in a hydrogen atmosphere are required. Based on these results, the ECS<sup>TM</sup> catalysts of interest were heat treated between 400°C to 1000°C in different atmospheres.

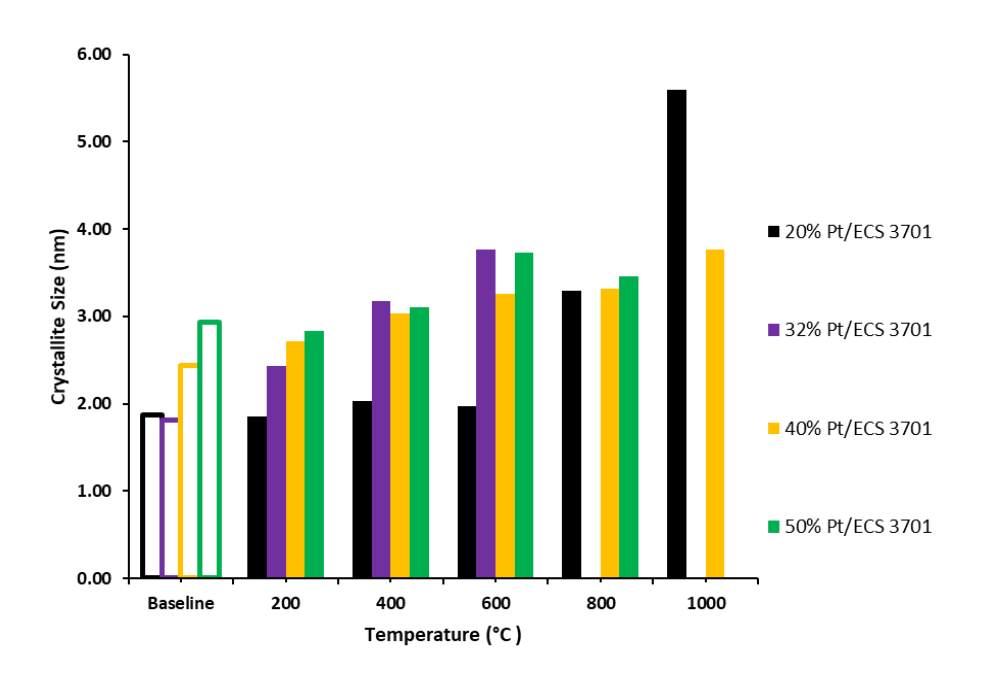


**Figure 3.** Crystallite size, based on (220) interplanar spacing, for Pt/ECS<sup>TM</sup> measured by XRD for different Pt loadings (from 20% to 50%).

The XRD spectra of the heat-treated samples at different atmospheres in Fig. 4 (a-c) show diffraction peaks at approximately 39°, 46°, 67°, and 81°, corresponding to Pt diffraction from (111), (200), (220), and (311) planes, respectively<sup>50</sup>. The bump around 25° corresponds to the carbon plane (002)<sup>51</sup>. Pt (220) reflection peak was used to calculate the Pt crystallite size because its intensity is the least affected by the reflections of the carbon support which overlaps with the

larger Pt (111) and Pt (200) Pt peaks<sup>38</sup>. As expected, an increase in the Pt crystallite size is observed as temperature increases for all atmospheres, see Table 1 and Figure 2(a). However, heat treatments at 1000°C in 7% H<sub>2</sub>/N<sub>2</sub> appear to have a stronger effect on Pt crystallite growth when compared to N<sub>2</sub> or Ar. The presence of hydrogen not only increases the mobility of Pt NPs on the carbon substrate but also the kinetics of the sintering and agglomeration<sup>36,49</sup>. It was also observed that Pt NPs growth was similar when these treatments were performed in both N<sub>2</sub> and Ar inert atmospheres. Similar to XRD, CO chemisorption characterization for 30 wt% Pt ECS<sup>TM</sup> catalysts showed a reduction of the Pt active metallic surface area pointing to the growth of the Pt NPs, see Table 1 and Figure 2 (b). Furthermore, the small presence of carbon crystallinity observed as a bump around 25° in the baseline samples and after 600°C heat treatments, was completely flattened after heat treatments at 1000°C, independently of the atmosphere. At the same time, the measured ECS<sup>TM</sup> interplanar spacing (d<sub>002</sub>) at 25° of the baseline samples and 600°C heat treated ones did not show considerable changes, with values around 3.50 Å, after heat treatments at 600°C. From the XRD data, it was not possible to measure d<sub>002</sub> samples after heat treatments at 1000°C due to the absence of carbon-associated peaks, making a detailed evaluation of the carbon crystallite sizes very difficult. Moreover, according to Franklin<sup>52</sup>,  $d_{002}$  values ~ 3.35 Å correspond to a single (ideal) graphite crystal with the highest graphitization degree, while values ~ 3.44 Å correspond to turbostratic or randomly oriented graphene layers with the lowest graphitization degree. However, Jia Ding et al.<sup>53</sup> stated some carbon structures with a mean d<sub>002</sub> larger than the equilibrium of graphite can also exhibit at some level an ordered structure with a mixture of graphitic and turbostratic stacking. In this research, the slight crystallinity of the ECS<sup>TM</sup> materials can be attributed to such a structure mixture. Whereas the noticeable decrease in ECSTM crystallinity can be related to the carbon decomposition under inert and reducing atmospheres at

1000°C during the 1 hr. long heat treatment. According to the literature, a continuous evolution of CO<sub>2</sub> and CO can be monitored when this type of carbon is exposed to a temperature range from 400°C to 1200°C<sup>54</sup>. The oxidation of the ECS<sup>TM</sup> also weakens the bonding and anchoring force between carbon and Pt nanoparticles, resulting in Pt nanoparticles detachment that can also lead to considerable Pt crystallite growth and agglomeration<sup>32</sup>, observed in Table 1.

**Table 2.**  $ECS^{TM}$  crystallite sizes.

Material	La (nm)	Material	La (nm)
Bare ECS <sup>TM</sup> 3701	4.31	Bare ECS <sup>TM</sup> 4601	4.23
30%Pt/ECS <sup>TM</sup> 3701, Baseline	4.44	30%Pt/ECS <sup>TM</sup> 4601, Baseline	4.36
30%Pt/ECS <sup>TM</sup> 3701, HT 600°C	4.19	30%Pt/ECS <sup>TM</sup> 4601, HT 600°C	4.31
30%Pt/ECS <sup>TM</sup> 3701, HT 1000°C	4.07	30%Pt/ECS <sup>TM</sup> 4601, HT 1000°C	4.07
30%Pt/ECS <sup>TM</sup> 3701, N <sub>2</sub> 600°C	4.44	30%Pt/ECS <sup>TM</sup> 4601, N <sub>2</sub> 600°C	4.36
30%Pt/ECS <sup>TM</sup> 3701, N <sub>2</sub> 1000°C	4.07	30%Pt/ECS <sup>TM</sup> 4601, N <sub>2</sub> 1000°C	4.07
30%Pt/ECS <sup>TM</sup> 3701, Ar 600°C	4.36	30%Pt/ECS <sup>TM</sup> 4601, Ar 600°C	4.36
30%Pt/ECS <sup>TM</sup> 3701, Ar 1000°C	3.89	30%Pt/ECS <sup>TM</sup> 4601, Ar 1000°C	4.11

The Raman characterization was used to estimate the amorphization or graphitization processes that might have taken place under the heat-treatment conditions. The Raman spectra for all samples are almost identical, having similar G and D1 band peaks for the baseline and heat-treated samples, see Figure 4 (d-f). The position of D1 peak (1350 cm<sup>-1</sup>) is the result of an amorphous or disordered carbon structure with structural imperfections and loss of symmetry, while G peak (1585 cm<sup>-1</sup>) represents the relative vibration of a more crystalline sp<sup>2</sup> hybridized carbon layers<sup>55</sup>. The broad hump in the second order region of the Raman spectra, between 2200 and 3400 cm<sup>-1</sup>, in these amorphous carbons seems to slightly increase as the heat treatment increases up to 1000 °C. According to literature, this feature observed in the Raman spectra of carbon (2400 and 3300 cm<sup>-1</sup>), can be explained by the presence of a mix of smaller graphitic and amorphous peaks<sup>56</sup>. However, without precise information on the nature of the peaks involved in these increments, it

would be challenging to associate the increase with graphitization or amorphization processes. Furthermore, the relative intensity ratios, R, show no obvious changes after Pt NPs dispersion on the ECS<sup>TM</sup>, see Table 1. This result implies no significant increment in the amount of defect sites on the surface of the carbon support by the addition of Pt, as stated in the literature<sup>57,58</sup>. Regarding the effect of the heat treatments on the carbon support, the peak ratios of the D1 and G modes (see Equation 2) for the ECS<sup>TM</sup> remained the same, around 1.00, after every heat treatment, implying no considerable change in the carbon structure toward either amorphization or graphitization, see Table 1 and Fig. 2 (c). These calculated D1 and G band intensity ratios are inversely proportional to the carbon's crystallite sizes, La, corresponding to the in-plane dimension of single crystalline domains in graphite<sup>43</sup>, see Equation 3. Table 2 shows how the La of bare ECS<sup>TM</sup> increases after Pt addition, while a continuous reduction is observed as temperature increases in the heat treated Pt/ECS<sup>TM</sup> samples. According to Marcinek et al.<sup>59</sup> the decrease in La can be accompanied by the broadening and high-frequency shifts of the G band translating to a loss of the crystallites long-range order and an increase in the point defect concentration.

Nevertheless, it must be emphasized that the interpretation of the Raman data is not straightforward. Each of the D1 and G values mentioned here was obtained by averaging five different Raman measurements obtained from different samples. While the shift values around the D1 band remained almost invariable and centered around 1350 cm<sup>-1</sup> for all samples. The shifts used to calculate the G band included values around 1585 cm<sup>-1</sup> as well as some values around 1600 cm<sup>-1</sup>, which are closer to the D2 (1610 cm<sup>-1</sup>) band in the Raman spectrum<sup>60</sup>. D2 represents the vibrational mode of disordered graphitic lattice-surface graphene layer that in many cases can interfere with the interpretation of the G band and subsequent assessments on graphitization<sup>61</sup>. This suggests a transition in the ECS<sup>TM</sup> material from mildly graphitized to a more amorphous carbon

structure. This is also an indication of the different degradation mechanisms and rates that the ECS<sup>TM</sup> can experience under the studied conditions, even though the variations in shift values between 1585 cm<sup>-1</sup> to 1600 cm<sup>-1</sup> were independent of changes in temperature and atmosphere. The detection of structural changes in these ECS<sup>TM</sup> materials only corroborated the presence of a relatively high density of site defect, inferred from the strong presence of D1 and D2 bands. This highly disordered carbon structure can provide an adequate interface for Pt migration and Pt NPs growth. However, the quantification of the carbon support structural qualities using D1, and G band intensity ratios only provides very limited insight, especially regarding the origin and nature of the structural defects.

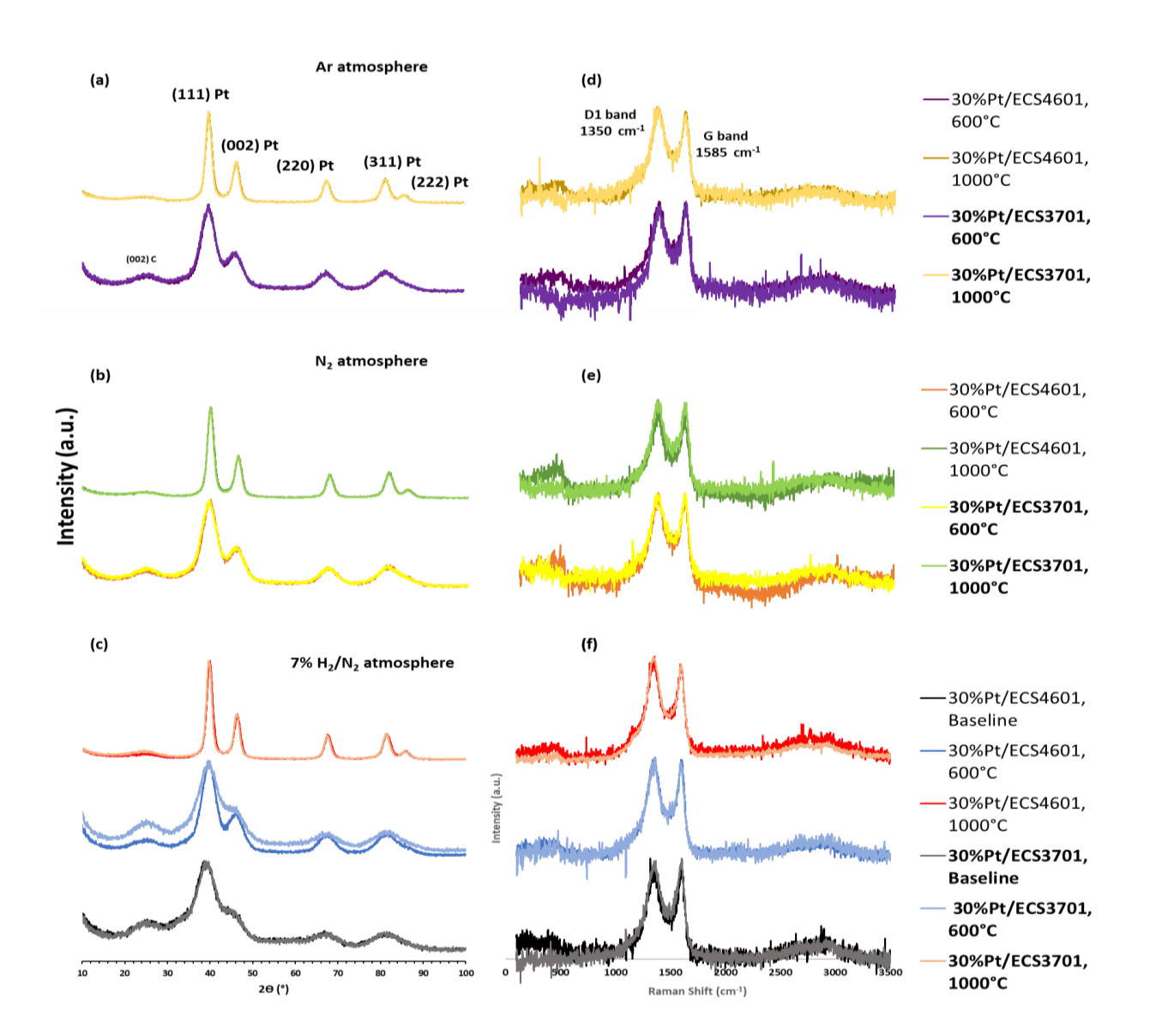


**Figure 4.** (a-c) XRD patterns for the baseline catalyst and heat-treated samples in (a) Ar, (b) N<sub>2</sub> and (c) 7%H<sub>2</sub>/N<sub>2</sub> atmospheres. Also, Raman spectra for the baseline catalyst and heat-treated samples in (d) Ar, (e) N<sub>2</sub> and (f) 7%H<sub>2</sub>/N<sub>2</sub> atmospheres.

Figure 5 shows the N<sub>2</sub> adsorption-desorption isotherms for the baseline and heat-treated Pt/ECS<sup>TM</sup> samples compared to the bare (no Pt) 3701 and 4601 ECS<sup>TM</sup> powders. According to the De Boer and Lippens category, they all displayed a type-IV isotherm, characteristic of strong

mesoporosity with pore sizes between 2-50 nm<sup>62</sup>. Also, according to the International Union of Pure and Applied Chemistry (IUPAC) the hysteresis loops suggest a combination of pore shapes regarded as wedge-shaped pores formed by the piling of flaky particles and slit-shape pores usually found in materials with lamellar structure. These hysteresis loops however, according to IUPAC classification, do not show well-developed cylinder-shaped pores that can better anchor Pt NPs and prevent their agglomeration<sup>63,64</sup>. Nonetheless, the mesoporosity of these carbon supports can function as a physical barrier to Pt NPs mobility and provide a good separation and encapsulation of the NPs without losing accessibility to the Pt active sites. Moreover, the BJH plots from Figure 5 (inset) show a bimodal pore diameter distribution for all samples, with a sharp peak present around 2-20 nm diameter, right at the mesopore scale, and a large hump at the macropore scale, around 50-120 nm diameter. This mesopores are large enough to encapsulate the Pt NPs.

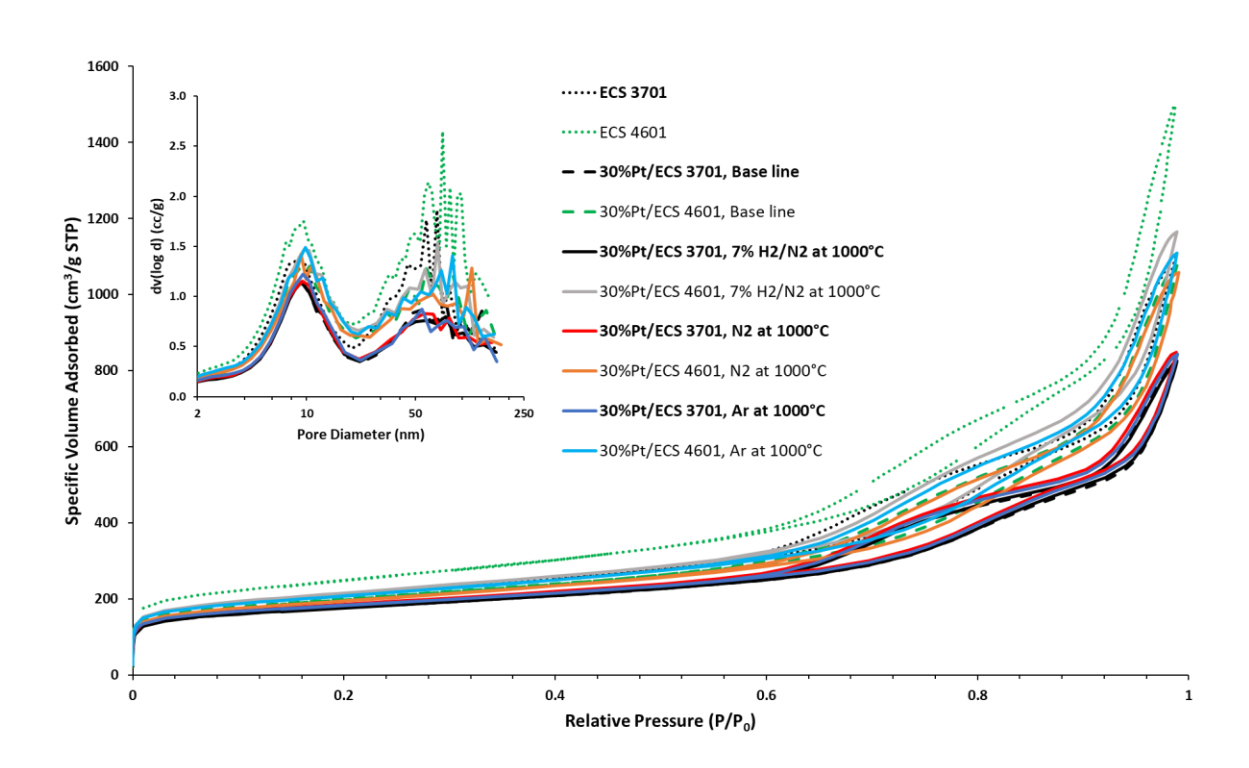


**Figure 5.** N<sub>2</sub> adsorption/desorption isotherms and (inset) pore-size distribution for the bare (no Pt) 3701 and 4601 ECS<sup>TM</sup> powder, the baseline Pt/ECS<sup>TM</sup> catalysts and heat-treated samples.

Figure 5 (inset) demonstrates that ECS<sup>TM</sup> without Pt has larger pore volume and surface area as well as a sharper pore-size distribution for both meso- and macropores (see Table 1 and Figure 2 (d-e)). However, the addition of Pt NPs tends to reduce, broaden, and flatten the hump representing macroporosity, while the intensity of the mesoporosity peaks is reduced as well, but not drastically. This reduction of macroporosity volume suggests that Pt NPs are more likely to be localized in the macropores, rather than inside the mesopores. However, additional characterization, such as three-dimensional (3D) TEM tomography, is needed to confirm this claim. Regarding the effect of the heat treatments, the studied conditions did not seem to induce large changes in the surface areas and porosity volume of the samples. The small variations in these values may be the result of removal/addition of impurities and the increase of Pt NPs.

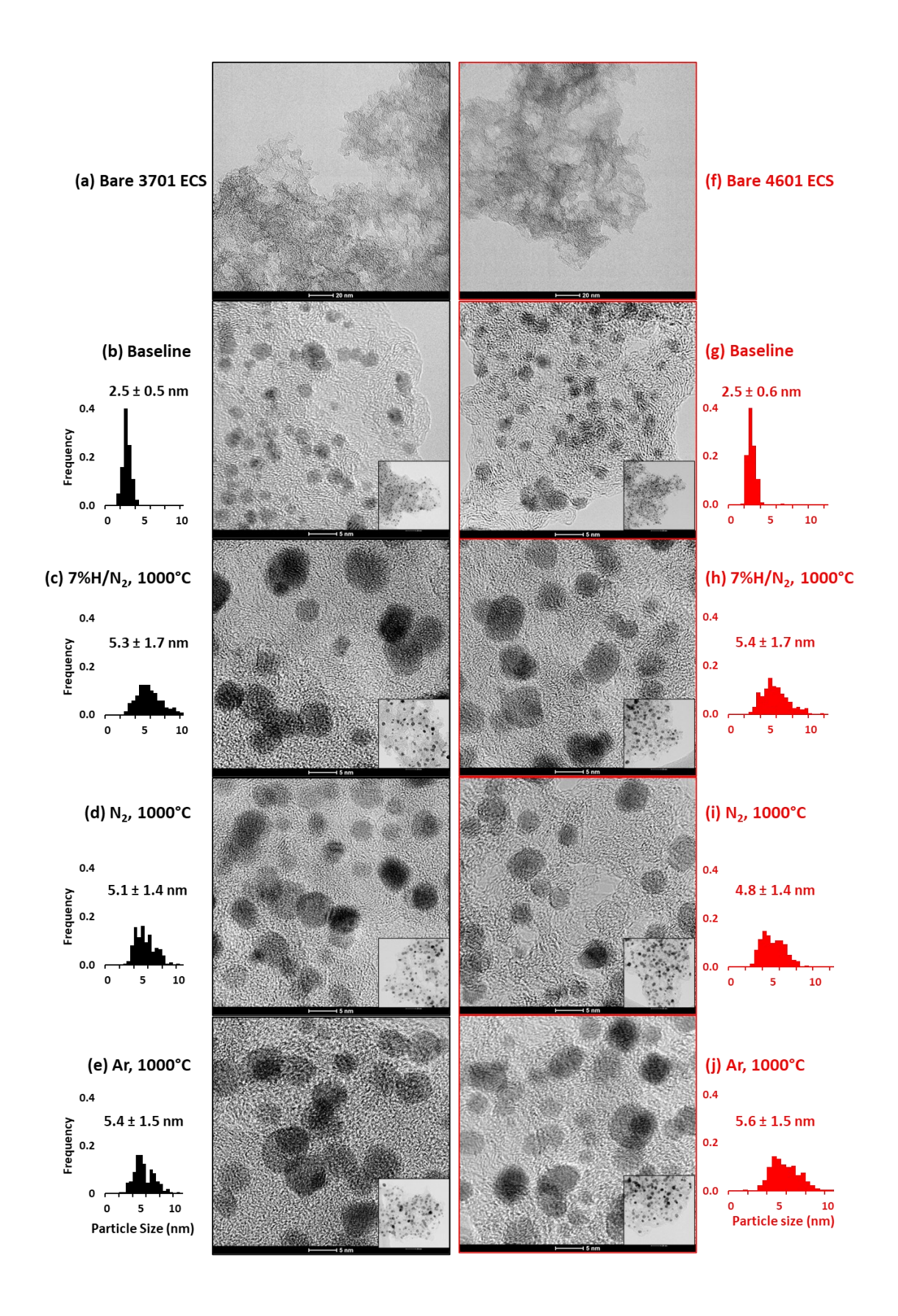


**Figure 6.** BF-TEM micrographs of bare carbons (a) ECS<sup>TM</sup> 3701 and (f) ECS<sup>TM</sup> 4601. BF-TEM micrographs include the corresponding PSD histograms of baseline 30% Pt/ECS<sup>TM</sup> (b) 3701 and (g) 4601 catalysts. Heat-treated samples at 1000°C in 7%H<sub>2</sub>/N<sub>2</sub> for 30% Pt/ECS<sup>TM</sup> (c) 3701 and (h) 4601 catalysts. Heat-treated samples at 1000°C in N<sub>2</sub> for 30% Pt/ECS<sup>TM</sup> (d) 3701 and (i) 4601 catalysts. Heat-treated samples at 1000°C in Ar for 30% Pt/ECS<sup>TM</sup> (e) 3701 and (j) 4601 catalysts. For simplicity, only TEM data from these specific treatments are shown here, however, this characterization was done on every sample after every heat treatment and the same trends were observed. Images framed in black represent ECS<sup>TM</sup> 3701 and 30%Pt/ECS<sup>TM</sup> 3701, while images framed in red represent ECS<sup>TM</sup> 4601 and 30%Pt/ECS<sup>TM</sup> 4601. The insets correspond to low magnification imaging to represent NPs dispersion.

The BF-TEM micrographs at different magnifications are displayed in Figure 6 (a-j), illustrating the NPs size changes under the heat treatment conditions. According to Asoro et al.<sup>30</sup> and Moldovan et al.<sup>31</sup>, the electron beam does not affect the sintering and coalescence of Pt NPs, hence the changes in the Pt particle sizes is assigned to the heat-treatment. The TEM micrographs of the bare ECS<sup>TM</sup>, the baseline catalysts and the heat-treated catalysts at 1000°C can be seen in Figure 6 (a-j). The examination of bare ECS<sup>TM</sup> 3701 and 4601 structures with TEM, Figure 6 (a and f), showed that the level of graphitization for ECS<sup>TM</sup> 3701 is very low for this amorphous carbon with flake-like structures and undiscernible lattice fringes, while for ECS<sup>TM</sup> 4601 some small level of graphitization was observed in the same flake-like structures. These subtle differences observed in TEM cannot be observed in the Raman spectra because of the difference in the resolution of the data acquired from both techniques. High resolution TEM (HRTEM) spatial resolution is ≤0.10 nm for Thermo Scientific<sup>TM</sup> TalosF200×200 kV and the spatial resolution for the Thermo DXR2

Raman spectrometer is lower, when equipped with a 532 nm diode laser. No changes caused by the beam were observed. When analyzing Pt/ECS<sup>TM</sup> powders, the structural changes of the heattreated catalysts at 400°C and 600°C were very minimal, similar to the small increase in crystallite sizes observed from XRD. For that reason, emphasis was placed on comparing the baseline catalysts only with the 1000°C heat-treated catalyst. Besides, under the TEM inspection, the Ptloaded ECS<sup>TM</sup> showed almost negligible changes after heat treatment. It can be concluded that the ECS<sup>TM</sup> structural changes and loss of carbon crystallinity inferred from XRD and Raman mainly occur in the interphase between the Pt NPs and the carbon support. This conclusion however can be validated by performing identical location TEM on these specific locations of the catalyst material<sup>65</sup>. The TEM micrographs and the corresponding PSD histograms for the baseline Pt loaded catalysts before heat treatments, Figure 6 (b and g), showed a homogenous and uniform (Gaussian-type) distribution of Pt NPs with the same mean PSD (2.5 nm) for both 3701 and 4601. After the heat treatments, Figure 6 (c-e and h-j), the histograms show a skewed Gaussian curve toward larger NP sizes with a uniformly distributed PSD. An increase in the Pt average particle size by a factor of 2 was observed for all samples after heat treatments at 1000°C, going from ~2.5 nm for the baseline catalyst to ~5nm. The mean particle size values measured by TEM are slightly higher than those of the crystallite sizes by XRD measurements (see Table 1). This only indicates the tendency for agglomeration of the Pt crystallites into NPs — one NP can be composed of just one single crystal or a numerous crystalline domain (crystallites). The PSD does not seem to be strongly affected by the different atmospheres, proving that temperature is the major driving force for the Pt NPs growth. It was also noticed that as these Pt NPs grow, independently of the heat treatment and atmosphere, the most prevalent facet of these Pt NPs was [111]. This was expected because at high temperatures Pt NPs have a strong tendency toward [111]-oriented crystallographic facets, with faceting starting to occur at about 400°C<sup>31</sup>. Moreover, from the histograms after heat treatments, the broadening of the PSD peak and the tail toward larger NP sizes (~10 nm) is characteristic of NP growth by agglomeration<sup>33</sup>. The increase of the mean particle size with temperature can also indicate sintering by coalescence, with Pt NPs migrating on the ECS<sup>TM</sup> to form clusters due to the degradation of not just the carbon support but also the Pt anchor sites to ECS<sup>TM 30</sup>. Another proposed mechanism is Ostwald ripening, where the dissolution of small Pt NPs is followed by its re-deposition on nearby and larger NPs, inducing the growth of the later<sup>31</sup>. In addition, Moldovan et al.<sup>31</sup> suggests that the Pt NPs experience partial melting at > 600°C leading to the formation of a highly mobile solid core NPs embedded in a liquid shell that wets the support surface facilitating Pt NPs migration and agglomeration.

Under BF-TEM, the visual inspection of oxidation was not possible, however, this analysis was performed by using FFT of the TEM micrographs. In addition, the goal was to determine if the heat treatment in different atmospheres affects the predominant Pt crystalline phases. The analysis was done on individual Pt NPs, to determine atomic interplanar spacing, see table 1. Figure 7 (a-h) shows representative micrographs in which atomic resolution can be resolved in some NPs along with their corresponding FFT patterns. For all samples, the FFT patterns of the Pt NPs reveal d-spacing that mostly corresponds to the crystalline planes (111) reflections of metallic Pt (FCC cubic structure) with also some presence of PtO<sub>2</sub> crystalline plane reflections at (310), (321) and (222). From our calculations, it was also noticed three different trends in oxidation: the oxide phase seemed to be more prevalent in the smaller Pt NPs (<2 nm), while in larger NPs (2 nm < PSD < 10 nm), both the oxide and metallic phases of Pt seem to coexist. However, in larger NPs (>10 nm) only the metallic phase was observed. This oxidation dependence on nanoparticle size was also concluded by Banerjee et al.<sup>66</sup>, stating that Pt NPs with very small average particle sizes tend

to exist as oxides only, and medium range particles exist as a core metal with a shell oxide structure, while the largest NPs are mainly metallic. Additionally, Sellin et al.<sup>54</sup> by studying the reactivity and degradation process of the carbon substrate under controlled temperatures and atmospheres similar to PEMFC operating at high temperatures. They stated that PtO surface species are generated from the thermal decomposition of Pt(OH)<sub>2</sub> at 150°C with H<sub>2</sub>O as a byproduct. These Pt surface oxide species can then catalyze ECS degradation processes under air and inert atmospheres by attacking the carbon at the interface between the Pt and the carbon support.

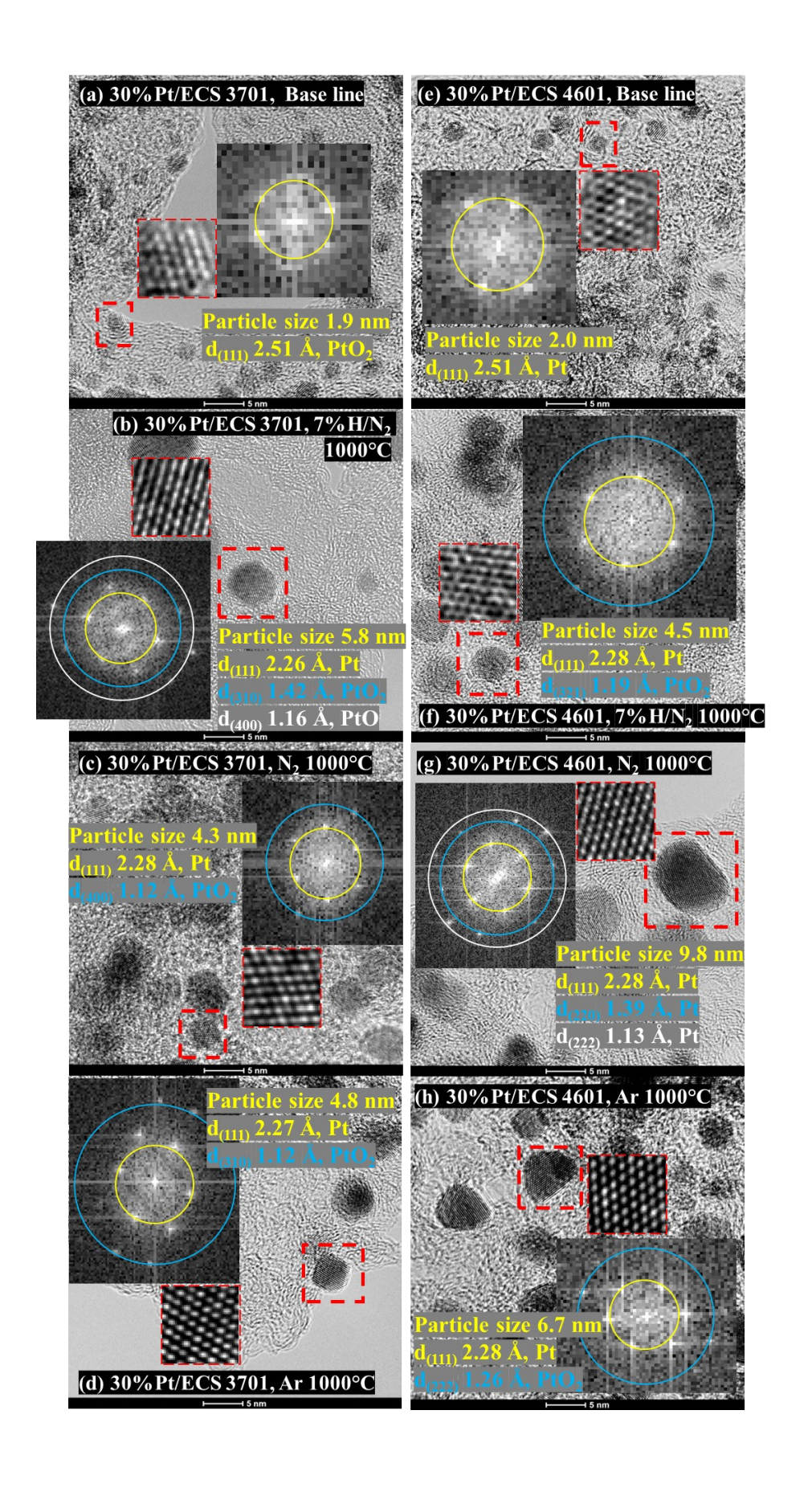


**Fig 7.** BF-TEM micrographs including insets of FFT patterns from a single NP (red dashed squares and their corresponding magnification) for baseline 30% Pt/ECS<sup>TM</sup> (a) 3701 and (e) 4601 catalysts, heat treated samples at 1000°C in 7%H<sub>2</sub>/N<sub>2</sub> for 30% Pt/ECS<sup>TM</sup> (b) 3701 and (f) 4601 catalysts, heat treated samples at 1000°C in N<sub>2</sub> for 30% Pt/ECS<sup>TM</sup> (c) 3701 and (g) 4601 catalysts, heat treated samples at 1000°C in Ar for 30% Pt/ECS<sup>TM</sup> (d) 3701 and (h) 4601 catalysts. Pt (111) represented the most prominent reflection on these NPs, even though Pt (222), PtO<sub>2</sub> (420), PtO<sub>2</sub> (200), PtO<sub>2</sub> (111), PtO<sub>2</sub> (311), among others, were also observed but in lower intensity.

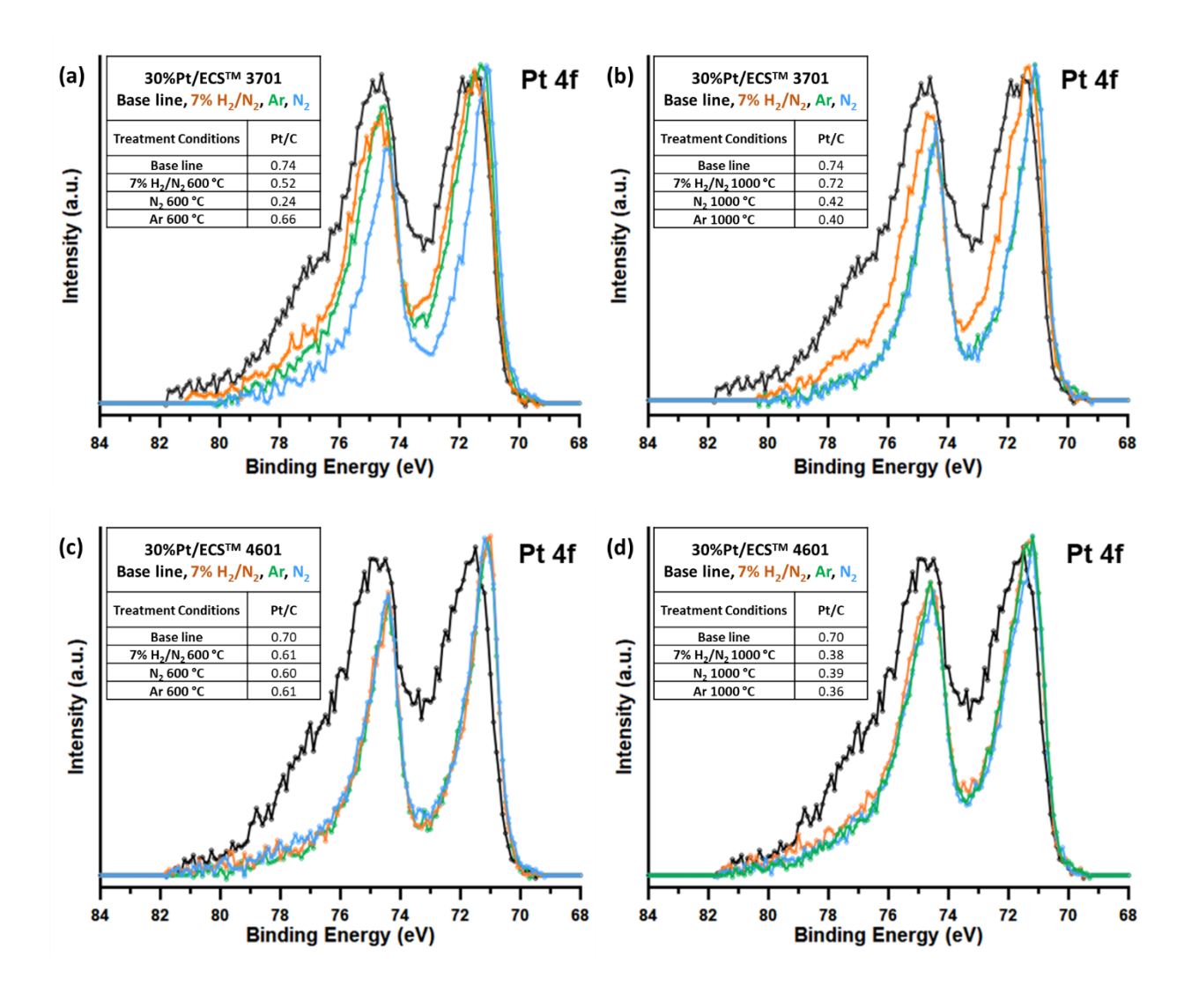


**Figure 8.** High-resolution XPS Pt 4f spectra of 30% Pt/ECS<sup>TM</sup> 3701 at (a) 600°C and (b) 1000°C and 30% Pt/ECS<sup>TM</sup> 4601 at (c) 600°C and (d) 1000°C in every studied atmosphere.

High-resolution XPS measurements provided confirmation and additional insights into the surface composition of the treated catalyst materials. From our previous research<sup>24</sup> it was concluded that bare ECS<sup>TM</sup> materials did not undergo any significant changes in carbon speciation (from analysis of C 1s spectra) after Pt NPs deposition, confirming that the addition of Pt NPs does not significantly affect the ECS<sup>TM</sup> surface chemistry. Figure 8 (a-d) shows the high-resolution Pt 4f spectra background subtracted and normalized at the 4f7/2 peak maximum located at ~71.1 eV, agreeing with reported values of the  $4f_{7/2}$  component for metallic Pt<sup>67</sup>. The XPS spectra revealed that for both sets of samples supported on  $ECS^{TM}$  3701 and 4601, the untreated catalysts are much more oxidized than the heat-treated ones. This is observed by peak width broadening indicative of greater contribution from PtO  $4f_{7/2}$  (~72.3 eV) and PtO<sub>2</sub>  $4f_{7/2}$  (~73.1 eV) after heat treatments<sup>68</sup>. The mean PSD of these catalyst materials is small enough in diameter to be measured in entirety by XPS, therefore the layer of oxide on the Pt surface (especially the baseline catalyst), have a large contribution to the Pt signal compared to lesser amount of bulk metallic Pt. According to Banerjee et al.<sup>66</sup>, the oxidized NPs are comprised of a metal core and an oxide shell so that the overall average size of Pt NPs would be the sum of the Pt metal and the oxide shell thicknesses. In addition, this can be correlated to our FFT analysis and the finding that the smaller particles tend to be more oxidized. XPS characterization also indicated that for the ECS 3701 series, N2 treatment was the most effective at decreasing the oxidation of Pt NPs to metallic state. This contradicts our expectation that the H<sub>2</sub>-containing atmosphere would be the most reducing one. Such finding could be explained by a small difference in Pt NP particle size distribution between

ECS 3701 treated in 7% H<sub>2</sub>/N<sub>2</sub> (having a broader PSD, with a higher contribution of small NP shown in our FFT to be oxidized), compared to ECS 3701 treated in N<sub>2</sub> (having a narrower PSD of NPs with mixed metallic and oxide state, as per our FFT analysis). However, more studies like in situ TEM and electron energy loss spectroscopy (EELS) are needed to bolster our conclusion. The decrease in the amount of oxidation from treatment seems to also yield a decrease in the total amount of Pt surface area which is shown in the elemental Pt/C ratios in Figure 8 (a-d) derived from the Pt 4f and C 1s core levels, and confirmed by CO chemisorption as agglomeration increases with temperature. At 1000°C, N2 and Ar are very similar in the amount of oxidation removed and this high temperature also follows the trends seen at 600°C, where more oxidation removed results in lower surface Pt. Lastly, in the overlays for the C1s, with similar maximum peak positions in all samples (about 284.5 eV), there was a very minor shift to higher binding energy in all treated powders compared to the untreated ones, less than 0.1 eV. This indicates that the heat treatments are slightly increasing the amount of sp<sup>3</sup> carbon nature, attributed to a diamondlike more amorphous carbon, and slightly decreasing the amount of sp<sup>2</sup>, characteristics of more graphitic carbon. This way, XPS is giving a more nuance examination of the small changes experienced by the carbon support that complements the XRD and Raman results.

# 4. CONCLUSION

In this research, heat treatments were performed on 30 wt% Pt catalysts supported on two different types on Engineered Catalyst Supports, ECS<sup>TM</sup>. Different temperatures ranging from 400°C to 1000°C were used in three different atmospheres, Ar, N<sub>2</sub> and a 7% H<sub>2</sub>/N<sub>2</sub> mixture. It was concluded that, for these materials and under these conditions, the temperature is the main factor controlling Pt NP growth, as shown by the increase in crystallite and particle size as a function of

temperature. However, the gases used in the atmosphere served to prevent the oxidation of Pt NPs

during the heat treatments, as revealed by XPS, from which N2 seemed to remove more oxygen

and to reduce the Pt NPs more effectively than the other two gases. Additionally, our FFT

calculation (from TEM micrographs) further revealed the effect of particle size on oxidation and

how the oxide phase tends to be more prevalent in smaller Pt NPs than in the larger ones. Regarding

the carbon support, the treatments did not produce any dramatic changes in the structure and

morphological characteristics of the carbon support as confirmed by Raman and N<sub>2</sub> physisorption

surface characterizations.

**AUTHOR INFORMATION** 

**Corresponding Author** 

Jasna Jankovic - Institute of Materials Science, University of Connecticut, Storrs, Connecticut

06269, United States; Email: jasna.jankovic@uconn.edu

**Author Contributions** 

The manuscript was written through contributions of all authors. All authors have given approval

to the final version of the manuscript.

**Funding Sources** 

National Science Foundation - Partnerships for Innovation in the track of Research Partnerships

program, award # 1919280.

Notes

31

The authors declare no competing financial interest.

#### ACKNOWLEDGMENT

This project was supported by the National Science Foundation through the Partnerships for Innovation award # 1919280 in the track of Research Partnerships program. Pajarito Powder LLC located in Albuquerque, New Mexico, was the provider of the catalyst materials and the facilities where the heat treatments were performed. Webb Johnson (from Pajarito Powder, LLC) for designing the schematic in Figure 1 and J. Kyle Keener for providing the photography of catalyst powder in Figure 1.

ABBREVIATIONS: PEM, proton exchange membrane; PEMFCs, proton exchange membrane fuel cells; ECS<sup>TM</sup>, engineered catalyst supports; MEA, membrane electrode assembly; HOR, hydrogen oxidation reaction; ORR, oxygen reduction reaction; NPs, nanoparticles; ASC, supermicroporous carbons (ASC); ECSA, electrochemically active surface area; XRD, X-ray diffraction; FWHM, full width at half maximum; BET, Brunauer–Emmett–Teller; BJH, Barrett–Joyner–Halenda; TEM, Transmission Electron Microscopy; BF-TEM, bright field TEM; HR-TEM, High resolution TEM; PSD, particle size distribution; FFT, Fast Fourier transform; XPS, X-ray Photoelectron Spectroscopy; IUPAC, International Union of Pure and Applied Chemistry.

#### REFERENCES

- 1. Mathias MF, Makharia R, Gasteiger HA, Conley JJ, Fuller TJ, Gittleman CJ, Kocha SS, Miller DP, Mittelsteadt CK, Xie T, Yan SG, Yu PT. Two Fuel Cell Cars In Every Garage? Electrochem Soc. Interface, 14, 24-35 (2005). doi: 10.1149/2.F05053IF.
- 2. Machol B, Rizk S. Economic value of U.S. fossil fuel electricity health impacts. Environ Int., 52, 75-80 (2013). doi:10.1016/j.envint.2012.03.003.
- 3. Akinyele D, Olabode E, Amole A. Review of fuel cell technologies and applications for sustainable microgrid systems. Inventions, 5(3), 1-35 (2020). doi:10.3390/inventions5030042.
- 4. El-Kharouf A, Chandan A, Hattenberger M, Pollet BG. Proton exchange membrane fuel cell degradation and testing: Review. Journal of the Energy Institute, 85(4), 188-200 (2012). doi:10.1179/1743967112Z.0000000036.
- 5. Garche J, Jörissen L. Applications of Fuel Cell Technology: Status and Perspectives. Electrochem Soc. Interface, 24, 39-43 (2015). doi:10.1149/2.F02152if.
- 6. Majlan EH, Rohendi D, Daud WRW, Husaini T, Haque MA. Electrode for proton exchange membrane fuel cells: A review. Renewable and Sustainable Energy Reviews, 89, 117-134 (2018). doi:10.1016/j.rser.2018.03.007.
- 7. Dicks AL. The role of carbon in fuel cells. J Power Sources, 156(2), 128-141 (2006). doi:10.1016/j.jpowsour.2006.02.054.
- 8. Sheng W. Electrocatalytic Activities of Supported Pt Nanoparticles for Low-Temperature Fuel Cell Applications. Massachusetts Institute of Technology; 2010.
- 9. Jayabal S, Saranya G, Geng D, Lin LY, Meng X. Insight into the correlation of Pt-support interactions with electrocatalytic activity and durability in fuel cells. J Mater Chem A Mater, 8(19), 9420-9446 (2020). doi:10.1039/d0ta01530j.
- 10. Ogungbemi E, Ijaodola O, Khatib FN, Wilberforce T, Hassan ZE, Thompson J, Ramadan M, Olabi AG. Fuel cell membranes Pros and cons. Energy, 172, 155-172 (2019). Doi:10.1016/j.energy.2019.01.034.
- 11. Hou J, Yang M, Ke C, Wie G, Priest C, Qiao Z, Wu G, Zhang J. Platinum-group-metal catalysts for proton exchange membrane fuel cells: From catalyst design to electrode structure optimization. Energy Chem, 2(1), 1-39 (2020). doi:10.1016/j.enchem.2019.100023.
- 12. Meier JC, Galeano C, Katsounaros I, Witte J, Bongard HJ, Topalov AA, Baldizzone C, Mezzavilla S, Schüth F, Mayrhofer KJJ. Design criteria for stable Pt/C fuel cell catalysts. Beilstein Journal of Nanotechnology, 5(1), 44-67 (2014). doi:10.3762/bjnano.5.5.
- 13. Moya X, Muñoz-Rojas D. Materials for Sustainable Energy Applications: Conversion, Storage, Transmission, and Consumption. Pan Stanford (2017).
- 14. Workman MJ, Dzara M, Ngo C, Pylypenko S, Serov A, McKinney S, Gordon J, Atanassov P, Artyushkova K. Platinum group metal-free electrocatalysts: Effects of synthesis on structure and performance in proton-exchange membrane fuel cell cathodes. J Power Sources, 348, 30-39 (2017). doi:10.1016/j.jpowsour.2017.02.067.

- 15. Asset T, Job N, Busby Y, Crisci A, Martin V, Stergiopoulos V, Bonnaud C, Serov A, Atanassov P, Chattot R, Dubau L, Maillard F. Porous Hollow PtNi/C Electrocatalysts: Carbon Support Considerations to Meet Performance and Stability Requirements. ACS Catal, 8(2), 893-903 (2018). doi:10.1021/acscatal.7b03539.
- 16. Ismagilov ZR, Kerzhentsev MA, Shikina NV, Lisitsyn AS, Okhlopkova LB, Barnakov Ch.N, Sakashita M, Iijima T, Tadokoro K. Development of active catalysts for low Pt loading cathodes of PEMFC by surface tailoring of nanocarbon materials. In: Catalysis Today, 102, 58-66 (2005). doi:10.1016/j.cattod.2005.02.007.
- 17. Gu K, Kim EJ, Sharma SK, Sharma PR, Bliznakov S, Hsiao BS, Rafailovich MH. Mesoporous carbon aerogel with tunable porosity as the catalyst support for enhanced proton-exchange membrane fuel cell performance. Mater Today Energy, 19, 1-9 (2021). doi:10.1016/j.mtener.2020.100560.
- 18. Marie J, Chenitz R, Chatenet M, Berthon-Fabry S, Cornet N, Achard P. Highly porous PEM fuel cell cathodes based on low density carbon aerogels as Pt-support: Experimental study of the mass-transport losses. J Power Sources, 190(2), 423-434 (2009). doi:10.1016/j.jpowsour.2009.01.047.
- 19. Ouattara-Brigaudet M, Berthon-Fabry S, Beauger C, Chatenet M, Job N, Sennour M, Achard P. Influence of the carbon texture of platinum/carbon aerogel electrocatalysts on their behavior in a proton exchange membrane fuel cell cathode. Int J Hydrogen Energy, 37(12), 9742-9757 (2012). doi:10.1016/j.ijhydene.2012.03.085.
- 20. Kaluža L, Larsen MJ, Zdražil M, Gulková D, Odgaard M. Fuel cell platinum catalysts supported on mediate surface area carbon black supports. Chem Eng Trans, 43, 913-918 (2015). doi:10.3303/CET1543153.
- 21. Paraknowitsch JP, Thomas A. Doping carbons beyond nitrogen: An overview of advanced heteroatom doped carbons with boron, sulphur and phosphorus for energy applications. Energy Environ Sci, 6(10), 2839-2855 (2013). doi:10.1039/c3ee41444b.
- 22. Zhou Y, Neyerlin K, Olson TS, Pylypenko S, Bult J, Dinh HN, Gennett T, Shao, Z, O'Hayre R. Enhancement of Pt and Pt-alloy fuel cell catalyst activity and durability via nitrogen-modified carbon supports. Energy Environ Sci, 3(10), 1437-1446 (2010). doi:10.1039/c003710a.
- 23. Shao Y, Sui J, Yin G, Gao Y. Nitrogen-doped carbon nanostructures and their composites as catalytic materials for proton exchange membrane fuel cell. Appl Catal B, 79(1), 89-99 (2008). doi:10.1016/j.apcatb.2007.09.047.
- 24. Dzara MJ, Godoy AO, Odgaard M, Zulevi B, Serov A, Jankovic J, Pylypenko S. Physicochemical Properties of ECS Supports and Pt/ECS Catalysts. ACS Appl Energy Mater, 4(9), 9111-9123 (2021). doi:10.1021/acsaem.1c01392.
- 25. Wood KN, O'Hayre R, Pylypenko S. Recent progress on nitrogen/carbon structures designed for use in energy and sustainability applications. In: Energy and Environmental Science. Royal Society of Chemistry, 7, 1212-1249 (2014). doi:10.1039/c3ee44078h.
- 26. Kim JY, Lee S, Kim TY, Pak C, Kim HT. Highly durable electrocatalyst with graphitized carbon supports modified by diazonium reaction for polymer

- electrolyte membrane fuel cell. Carbon N Y, 77, 525-537 (2014). doi:10.1016/j.carbon.2014.05.058.
- 27. Banham D, Feng F, Fürstenhaupt T, Pei K, Ye S, Birss V. Novel mesoporous carbon supports for PEMFC catalysts. Catalysts, 5(3), 1046-1067 (2015). doi:10.3390/catal5031046.
- 28. Park SJ, Kim BJ, Lee SY. Effect of surface modification of mesoporous carbon supports on the electrochemical activity of fuel cells. J Colloid Interface Sci, 405, 150-156 (2013). doi:10.1016/j.jcis.2013.04.009.
- 29. Urchaga P, Weissmann M, Baranton S, Girardeau T, Coutanceau C. Improvement of the platinum nanopartides-carbon substrate interaction by insertion of a thiophenol molecular bridge. Langmuir, 25(11), 6543-6550 (2009). doi:10.1021/la9000973.
- Asoro MA, Kovar D, Shao-Horn Y, Allard LF, Ferreira PJ. Coalescence and sintering of Pt nanoparticles: in situ observation by aberration-corrected HAADF STEM. Nanotechnology, 21(2), 025701 (2010). doi:10.1088/0957-4484/21/2/025701.
- 31. Moldovan MS, Bulou H, Dappe YJ, Janowska I, Bégin D, Pham-Huu C, Ersen O. On the evolution of Pt nanoparticles on few-layer graphene supports in the high-temperature range. Journal of Physical Chemistry C, 116(16), 9274-9282 (2012). doi:10.1021/jp2124235.
- 32. Zhang S, Yuan XZ, Hin JNC, Wang H, Friedrich KA, Schulze M. A review of platinum-based catalyst layer degradation in proton exchange membrane fuel cells. J Power Sources, 194(2), 588-600 (2009). doi:10.1016/j.jpowsour.2009.06.073.
- 33. Meier JC, Galeano C, Katsounaros I, Topalov AA, Kostka A, Schüth F, Mayrhofer KJJ. Degradation mechanisms of Pt/C fuel cell catalysts under simulated start-stop conditions. ACS Catal, 2(5), 832-843 (2012). doi:10.1021/cs300024h.
- 34. Hartl K, Hanzlik M, Arenz M. IL-TEM investigations on the degradation mechanism of Pt/C electrocatalysts with different carbon supports. Energy Environ Sci, 4(1), 234-238 (2011). doi:10.1039/c0ee00248h.
- 35. Calvillo L, Gangeri M, Perathoner S, Centi G, Moliner R, Lázaro MJ. Effect of the support properties on the preparation and performance of platinum catalysts supported on carbon nanofibers. J Power Sources, 192(1), 144-150 (2009). doi:10.1016/j.jpowsour.2009.01.005.
- 36. Vleeming JH, Kuster BFM, Marin GB, Oudet F, Courtine P. Graphite-Supported Platinum Catalysts: Effects of Gas and Aqueous Phase Treatments. Journal Of Catalysis, 166, 148–159 (1997). doi:10.1006/JCAT.1997.1489.
- 37. Xu JB, Zhao TS. Mesoporous carbon with uniquely combined electrochemical and mass transport characteristics for polymer electrolyte membrane fuel cells. RSC Adv, 3(1), 16-24 (2013). doi:10.1039/c2ra22279e.
- 38. Sevjidsuren G, Zils S, Kaserer S, Wolz A, Ettingshausen F, Dixon D, Schoekel A, Roth C, Altantsog P, Sangaa D, Ganzorig Ch. Effect of different support morphologies and Pt particle sizes in electrocatalysts for fuel cell applications. J Nanomater, 2010, 1-9 (2010). doi:10.1155/2010/852786.
- 39. Pajarito Powder L. Engineered Catalyst SupportsTM. https://pajaritopowder.com/products/. July (2023).

- 40. Hargreaves JSJ. Some considerations related to the use of the Scherrer equation in powder X-ray diffraction as applied to heterogeneous catalysts. Catalysis, Structure and Reactivity, 2(1-4), 33-37 (2016). doi:10.1080/2055074X.2016.1252548.
- 41. Wang V, Alsmeyer DC, Mccreery RL. Raman Spectroscopy of Carbon Materials: Structural Basis of Observed Spectra. Chem Mater, 2, 557-563 (1990). doi.org/10.1021/cm00011a018.
- 42. Schwan J, Ulrich S, Batori V, Ehrhardt H, Silva SRP. Raman spectroscopy on amorphous carbon films. J Appl Phys, 80(1), 440-447 (1996). doi:10.1063/1.362745.
- 43. Cornaglia LM, Múnera J, Irusta S, Lombardo EA. Raman studies of Rh and Pt on La<sub>2</sub>O<sub>3</sub> catalysts used in a membrane reactor for hydrogen production. Appl Catal A Gen, 263(1), 91-101 (2004). doi:10.1016/j.apcata.2003.12.003.
- 44. Weidenthaler C. Pitfalls in the characterization of nanoporous and nanosized materials. Nanoscale, 3(3), 792-810 (2011). doi:10.1039/c0nr00561d.
- 45. Khosrowshahi MS, Abdol MA, Mashhadimoslem H, Khakpour E, Motejadded-Emrooz HB, Sadeghzadeh S, Ghaemi A. The role of surface chemistry on CO2 adsorption in biomass-derived porous carbons by experimental results and molecular dynamics simulations. Sci Rep, 12 (1), 1-19 (2022). doi:10.1038/s41598-022-12596-5.
- 46. Tanhaei B, Ayati A, Iakovleva E, Sillanpää M. Efficient carbon interlayed magnetic chitosan adsorbent for anionic dye removal: Synthesis, characterization and adsorption study. Int J Biol Macromol, 164, 3621-3631 (2020). doi:10.1016/j.ijbiomac.2020.08.207.
- 47. Bardestani R, Patience GS, Kaliaguine S. Experimental methods in chemical engineering: specific surface area and pore size distribution measurements—BET, BJH, and DFT. Canadian Journal of Chemical Engineering, 97(11), 2781-2791 (2019). doi:10.1002/cjce.23632.
- 48. Borghi F, Milani M, Bettini LG, Podestà A, Milani P. Quantitative characterization of the interfacial morphology and bulk porosity of nanoporous cluster-assembled carbon thin films. Appl Surf Sci, 479, 395-402 (2019). doi:10.1016/j.apsusc.2019.02.066.
- 49. Bett JAS, Kinoshita K, Stonehaht P. Crystallite Growth of Platinum Dispersed on Graphitized Carbon Black II. Effect of Liquid Environment. Journal of Catalysis, 41, 124-133 (1976). doi: 10.1016/0021-9517(76)90207-4.
- 50. Evangelista TCS, Paganoto GT, Guimarães MCC, Ribeiro J. Raman spectroscopy and electrochemical investigations of pt electrocatalyst supported on carbon prepared through plasma pyrolysis of natural gas. Journal of Spectroscopy, 2015, 1-7 (2015). doi:10.1155/2015/329730.
- 51. Zickler GA, Smarsly B, Gierlinger N, Peterlik H, Paris O. A reconsideration of the relationship between the crystallite size La of carbons determined by X-ray diffraction and Raman spectroscopy. Carbon N Y, 44(15), 3239-3246 (2006). doi:10.1016/j.carbon.2006.06.029.
- 52. Rosalind E. Franklin. Crystallite growth in graphitizing and non-graphitizing carbons. Royal Society, 209, 196-218 (1947). doi.org/10.1098/rspa.1951.0197.
- 53. Ding J, Wang H, Li Z, Kohandehghan A, Cui K, Xu Z, Zahiri B, Tan X, Lotfabad EM, Olsen BC, Mitlin D. Carbon nanosheet frameworks derived from peat moss as

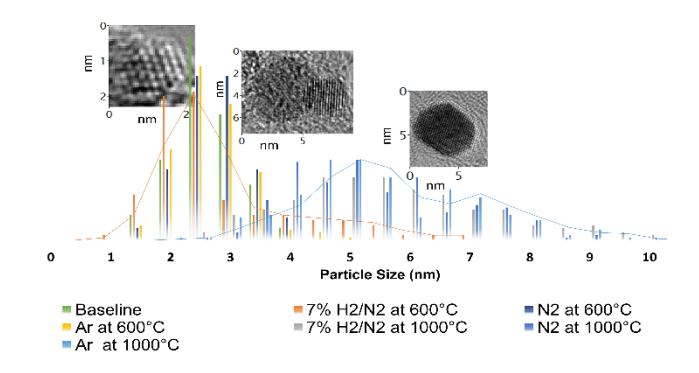
- high performance sodium ion battery anodes. ACS Nano, 7(12), 11004-11015 (2013). doi:10.1021/nn404640c.
- 54. Sellin R, Clacens JM, Coutanceau C. A thermogravimetric analysis/mass spectroscopy study of the thermal and chemical stability of carbon in the Pt/C catalytic system. Carbon, 48(8), 2244-2254 (2010). doi:10.1016/j.carbon.2010.02.034.
- 55. Sadezky A, Muckenhuber H, Grothe H, Niessner R, Pöschl U. Raman microspectroscopy of soot and related carbonaceous materials: Spectral analysis and structural information. Carbon. 43(8), 1731-1742 (2005). doi:10.1016/j.carbon.2005.02.018.
- 56. Lee YJ. The second order Raman spectroscopy in carbon crystallinity. Journal of Nuclear Materials. 325(2-3), 174-179 (2004). doi:10.1016/j.jnucmat.2003.12.005.
- 57. Shanahan P V., Xu L, Liang C, Waje M, Dai S, Yan YS. Graphitic mesoporous carbon as a durable fuel cell catalyst support. J Power Sources. 185(1), 423-427 (2008). doi:10.1016/j.jpowsour.2008.06.041.
- 58. Wang JN, Zhao YZ, Niu JJ. Preparation of graphitic carbon with high surface area and its application as an electrode material for fuel cells. J Mater Chem. 17(21), 2251-2256 (2007). doi:10.1039/b700147a.
- 59. Marcinek M, Hardwick LJ, Zukowska GZ, Kostecki R. Microwave plasma chemical vapor deposition of graphitic carbon thin films. Carbon. 48(5), 1552-1557 (2010). doi:10.1016/j.carbon.2009.12.052.
- 60. Jawhari T, Roid A, Casado J. Raman Spectroscopic Characterization Of Some Commercially Available Carbon Black Materials. Carbon. 33(11), 1561-1565 (1995). doi: 10.1016/0008-6223(95)00117-V.
- 61. Hara M, Lee M, Liu CH, Cheng BH, Yamashita Y, Uchida M, Uchida H, Watanabe M. Electrochemical and Raman spectroscopic evaluation of Pt/graphitized carbon black catalyst durability for the start/stop operating condition of polymer electrolyte fuel cells. Electrochim Acta. 70, 171-181 (2012). doi:10.1016/j.electacta.2012.03.043.
- 62. Lowell S, Shields JE, Thomas MA, Thommes M. Characterization of Porous Solids and Powders: Surface Area, Pore Size and Density. Springer Netherlands, 16 (2004). doi:10.1007/978-1-4020-2303-3.
- 63. Sing KSW, Everett DH; Haul RAW, Moscou L, Pierotti RA, Rouquerol J, Siemieniewska T. Reporting Physisorption Data for Gas/Solid Systems With Special Reference To The Determination Of Surface Area And Porosity. Pure and Applied Chemistry, 54(11), 2201-2218 (1982). doi: 10.1351/pac198254112201.
- 64. Thommes M, Kaneko K, Neimark A V., Oliver JP, Rodriguez-Reinoso F, Rouquerol J, Sing KSW. Physisorption of gases, with special reference to the evaluation of surface area and pore size distribution (IUPAC Technical Report). Pure and Applied Chemistry, 87(9-10), 1051-1069 (2015). doi:10.1515/pac-2014-1117.
- 65. Lafforgue C, Maillard F, Martin V, Dubau L, Chatenet M. Degradation of Carbon-Supported Platinum-Group-Metal Electrocatalysts in Alkaline Media Studied by in Situ Fourier Transform Infrared Spectroscopy and Identical-Location Transmission Electron Microscopy. ACS Catal. 9, 5613-5622 (2019). doi:10.1021/acscatal.9b00439.

- 66. Banerjee R, Liu Q, Tengco JMM, Regalbuto JR. Detection of Ambient Oxidation of Ultrasmall Supported Platinum Nanoparticles with Benchtop Powder X-Ray Diffraction. Catal Letters, 147(7), 1754-1764 (2017). doi:10.1007/s10562-017-2060-2.
- 67. Miller DJ, Øberg H, Kaya S, Sanchez Casalongu H, Friebel D, Anniyev T, Ogasawara H, Bluhm H, Pettersson LGM, Nilsson A. Oxidation of Pt(111) under near-ambient conditions. Phys Rev Lett, 107(19), 1-5 (2011). doi:10.1103/PhysRevLett.107.195502.
- 68. Baranova EA, Artyushkova K, Halevi B, Amir T, Martinez U, Atanassov P. Pt7Sn3 Catalysts for Ethanol Electro-Oxidation: Correlation between Surface Structure and Catalytic Activity. ECS Trans, 41(1), 1691-1700 (2011). doi:10.1149/1.3635700.

# TABLE OF CONTENTS

ABS	STRACT	1
1.	INTRODUCTION	2
2.	EXPERIMENTAL	7
2.1.	Heat treatment:	7
2.2.	Physicochemical Characterization:	7
3.	RESULTS AND DISCUSSION:	11
4.	CONCLUSION	30
AUT	THOR INFORMATION	31
ACK	KNOWLEDGMENT	32
ABB	BREVIATIONS	32
DFF	TEDENCES	22

# TOC Journal format:



# TOC enlarged:

